Dalai, B., Kumar, P., Yuan, X. (2019): De-noising receiver function data using the Seislet Transform. - *Geophysical Journal International*, *217*, 3, pp. 2047—2055.

DOI: http://doi.org/10.1093/gji/ggz135

Geophysical Journal International

Geophys. J. Int. (2019) **217,** 2047–2055
Advance Access publication 2019 March 14
GJI Seismology

doi: 10.1093/gji/ggz135

De-noising receiver function data using the Seislet Transform

Bijayananda Dalai,[1,2] Prakash Kumar[1] and Xiaohui Yuan[3]

[1]*CSIR- National Geophysical Research Institute, Uppal Road, Hyderabad 500007, India. E-mail: prakashk@ngri.res.in*
[2]*AcSIR – National Geophysical Research Institute, Hyderabad, India*
[3]*Deutsches GeoForchungsZentrum GFZ, Telegrafenberg, Potsdam 14473, Germany*

Accepted 2019 March 12. Received 2019 February 28; in original form 2018 July 13

SUMMARY

The converted wave data (*P*-to-*s*/*S*-to-*p*), commonly termed as receiver functions, contain noise of various origins. Such noises may influence the modeling and may sometimes lead to over interpretations of the data. In order to suppress noise, we use a robust sparsity enhancing tool, that is, the Seislet Transform, to process receiver function data by applying regularization in the seislet domain. The transform utilizes the multiscale orthogonal basis and the basis functions are oriented along the dominant seismic phases following local linearity. The inversion results of both the synthetic and field examples from the Hi-CLIMB network and station HYB from the Indian shield show an excellent performance over the original data sets.

Key words: Asia; Body waves; Computational seismology; Crustal imaging; Seismic noise.

1 INTRODUCTION

The converted wave technique, traditionally called receiver function (RF; e.g. Burdick & Langston 1977; Langston 1977; Vinnik 1977), has been proved to be a robust tool to image crust and upper-mantle discontinuities. The receiver functions can be defined as Green's functions that are closely associated with structures beneath the seismic stations and can be retrieved from three component seismograms. Receiver function data, like any other seismic wavefields, contain noise of various origins, for example, background noise, filter induced noise and migration smiles. In exploration seismology, seismic data processing is an inevitable workflow to enhance the signal-to-noise ratio (SNR) by utilizing sophisticated seismic imaging algorithms (Yilmaz 2001). Many of these array-based data pre-processing techniques are also applicable in teleseismic wavefield imaging. Exploration geophysicists have developed many de-noising schemes to regularize the irregular seismic data (e.g. Kanasewich *et al.* 1973; Tessmer & Behle 1988; Poppeliers & Pavlis 2003; Abma & Kabir 2005). The approximate plane-wave feature of teleseismic wave front ensures a smoothness of teleseismic data, which facilitates the wavefield reconstruction. Therefore, some robust methods, such as weighted slant stacking (e.g. Neal & Pavlis 1999; Poppeliers & Pavlis 2003; Pavlis 2011) and cubic B-spline interpolation (e.g. Sheldrake *et al.* 2002; Zhang & Zheng 2015), have been applied to teleseismic wavefield reconstruction to improve the SNR. Additionally, there exist various sparsity promoting transforms, for example, Wavelet transform (Mallat 2009), Curvelets (Starck *et al.* 2002), Shearlets (Guo & Labate 2007), Basis pursuit deconvolution (e.g. Chen *et al.* 1998; Sen *et al.* 2014), Radon transform (Foster & Mosher 1992), Empirical wavelet transforms (Liu *et al.* 2016), etc. In general, the Wavelet transform has poor directionality and does not provide shift variance, as a result of which it cannot capture the curves and edges of a constructed image precisely. The Curvelet transform deals with curves and edges as it is characterized by both direction and scale; therefore, it simultaneously provides a sparse representation of the complex seismic data (Hermann *et al.* 2007). However, it has high computational cost and also the choice of thresholding value is crucial. Furthermore, it does not take into account the prior knowledge of the seismic data. Another transform, Shearlet, is also multiscale directional, which accommodates various geometrical features; however, it may sometime introduce artifacts. The Basis pursuit deconvolution method utilizes sparse inversion techniques, which is accommodated with a regularization parameter, but the choice of this parameter is an open problem. The Radon transform is also a sparsity promoting tool, which is based on the shape of the integral operator and can be utilized using linear, parabolic, hyperbolic and polynomial functions (Xue *et al.* 2014, 2016). On the other hand, the Seislet Transform (ST; Fomel & Liu 2010) is characterized by the use of plane wave destruction(PWD) filter (Claerbout 1992), which acts as local slope estimator assuming piecewise linear signal from the input data set. Therefore, it is intimately dependent on the local slope estimation instead of input parameters and has more multiscale sparse compared to other transforms (Chen & Fomel 2018). Among different random noise attenuation approaches, the ST domain thresholding approach has emerged as one of the most widely used approach (Chen 2016). The principle of this approach is simple, that is, seismic phase has coherent structure and can be sparsely represented, while random noise is spreading through the whole transform domain, thus can be removed by applying a simple thresholding operator in the transformed domain. Slope estimation is a process that predicts the seismic phase between adjacent traces throughout a seismic profile using an operator. The ST method can effectively compress and separate the data up to a certain degree of accuracy

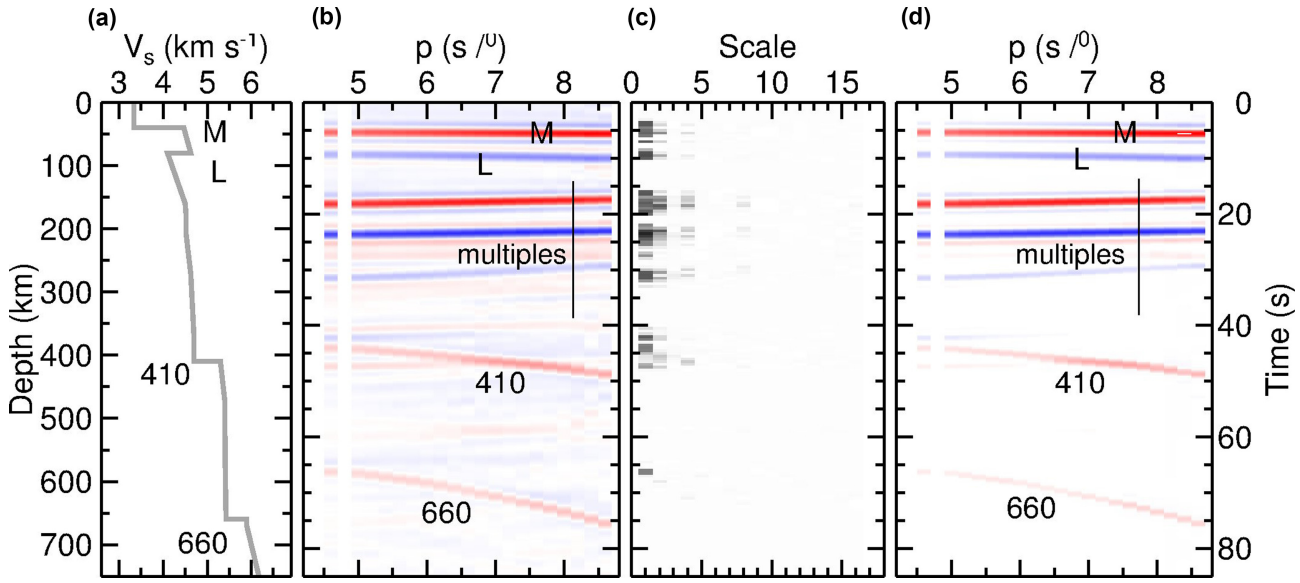

Figure 1. Analysis of synthetic RF data in the seislet domain. The synthetic RFs have been generated using the reflectivity method for a simple model shown in panel (a). (b) The RF images shows four primary converted phases (labelled as M, L, 410 and 660) and free surface reverberations mostly occurring below 10 s time window. Panel (c) denotes the Seislet Transform generated using forward ST with significant coefficients of 20%. The abscissa represents the distance separation between the traces. The reconstructed image using the inverse ST is displayed in panel (d), which shows remarkable improvement by subsiding the noise from various origins.

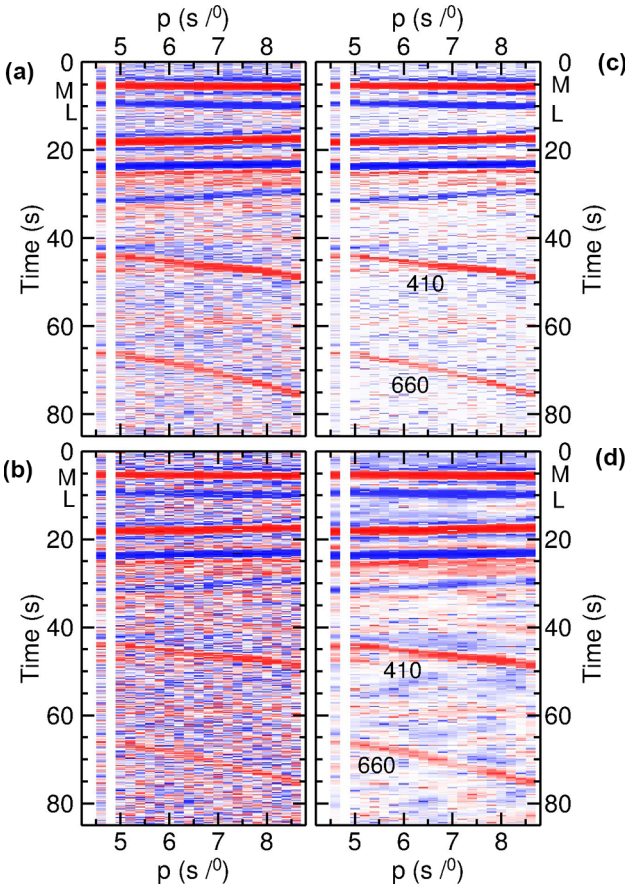

Figure 2. Same as Fig. 1 but the synthetic RF data are now contaminated with two different amounts of Gaussian noise with 7% (a) and 10% (b), respectively. The resulting reconstructed images for the two cases are depicted in panels (c) and (d), respectively. It is clearly seen that the signal-to-noise ratio of the reconstructed images is improved.

based on their difference in local slopes and therefore stands hybrid for attenuating random noise by simply applying a thresholding for most significant coefficients (Donoho 1995; a structural filtering approach).

In this study we use the ST to a suit of synthetic receiver function data as well as the real field data from Hi-CLIMB network in the Nepal Himalayan region and from a GEOSCOPE station (HYB) located in the Precambrian shield of central India. The reconstructed images show an excellent improvement of the noise attenuation over the original ones.

2 METHODOLOGY

The ST is widely used in reflection seismology to improve the sparsity regularization (Xue *et al.* 2017). Basically, the ST is a robust de-noising technique that takes the advantage of the local slope estimation using the plane-wave destruction filter (Fomel 2002). Further, it is one kind of special *wavelet like transform* for seismic data, which has more effective compression capability than the classical wavelet transform. In practice we can define the seismic data as collections of traces and predict one trace from the other by only following the local seismic event slopes. Such prediction process carried out by plane-wave destruction is the key idea in the ST (Fomel 2002). The details of the ST have been given by Fomel & Liu (2010); however, for the sake of completeness we briefly describe here the key steps.

Here, we applied a 2D ST to RF data. The approach consists of forward and inverse processes. The RF amplitude data can be viewed as a collection of traces (sequence) and one trace can be predicted from others on the basis of local slopes of the seismic phases. The local slope can be calculated using a robust algorithm as introduced by Fomel (2002). The sequence of RF amplitude data is divided into odd (o) and even (e) parts and one part will be predicted from the other. The next step is to find the residual difference r between the odd component and the prediction of odd component from the even

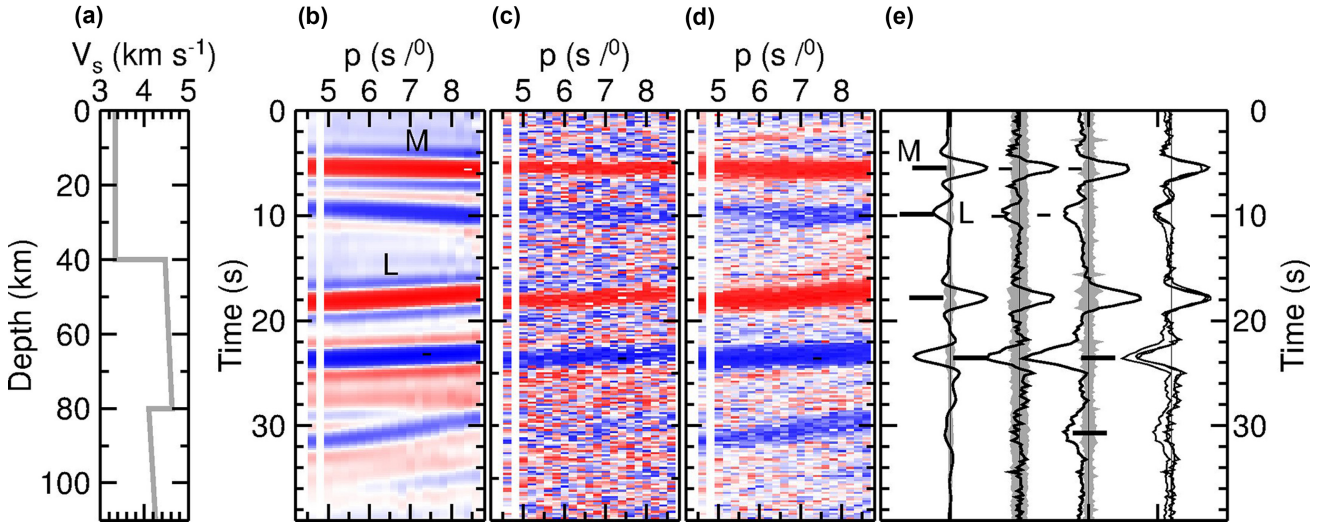

Figure 3. Same as Fig. 1 but the synthetic RF data (b) are now contaminated with 10% Gaussian noise (c). Here the model is taken up to the upper most mantle depth with Moho at 40 km depth and an LVL at 80 km depth (a). RFs contain primary converted phases between 4 and 11 s and free surface reverberations (between 15 and 32 s). The inverse ST image has been displayed in panel (d), which has marked improvement over the original. Panel (e) shows the stack traces generated after the moveout correction with the reference slowness of 6.4 s deg^{-1}. The stack traces are displayed in the same order as the images are arranged. In order to show that insignificant pulse broadening has taken place, all the individual stacked traces are superimposed and plotted in panel (e) at the rightmost. The two thin parallel lines on the summation traces are the errors estimated with bootstrap technique with $\pm 2\sigma$ standard error limit. It is clearly seen that the stack trace as well as the image of the reconstructed data brought out the desired phases as inferred from the model very well above the noise level.

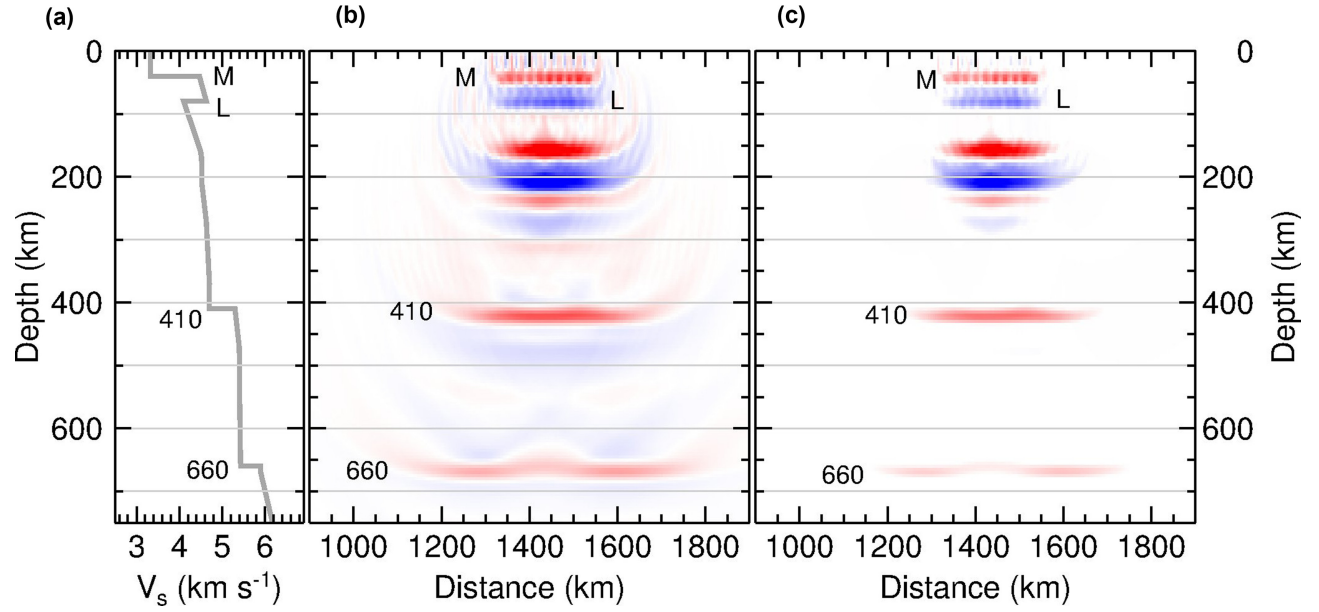

Figure 4. The analysis of migrated RF data in the seislet domain. (a) The velocity model of the upper mantle for generating the synthetic RFs. (b) The RF cross-section using the Fresnel zone migration. (c) Reconstruction of the migrated RF cross-section. The spurious noise and smiley effect generated by the hyperbola are substantially reduced.

component, that is,

$$r = \mathrm{o} - P\,[\mathrm{e}]\,, \tag{1}$$

where P is a prediction operator and it can be defined as

$$P[e]_K = (R_k^{(+)}[e_{k-1}] + R_k^{(-)}[e_k])/2, \tag{2}$$

where e_k is the even components of RF data at the kth transform scale, $R_k^{(+)}$ and $R_k^{(-)}$ are operators that predict a trace from its left and right neighbours correspondingly by shifting seismic events according to their slopes. A good prediction operator leaves the residual small. Here we use the Cohen–Daubechies–Feauveau bi-orthogonal wavelet (Cohen *et al.* 1992), as it is a basic algorithm for the lifting scheme and fits the de-noising theory in the seislet domain better than other wavelets. Next, the coarse approximation c has been estimated from the RF data by updating the even component,

$$c = \mathrm{e} + U\,[r]\,, \tag{3}$$

where, U is the update operator which preserves the running average of the signal (Sweldens & Schroder 1996), and can be defined as

$$U[r]_K = (R_k^{(+)}[r_{k-1}] + R_k^{(-)}[r_k])/4, \tag{4}$$

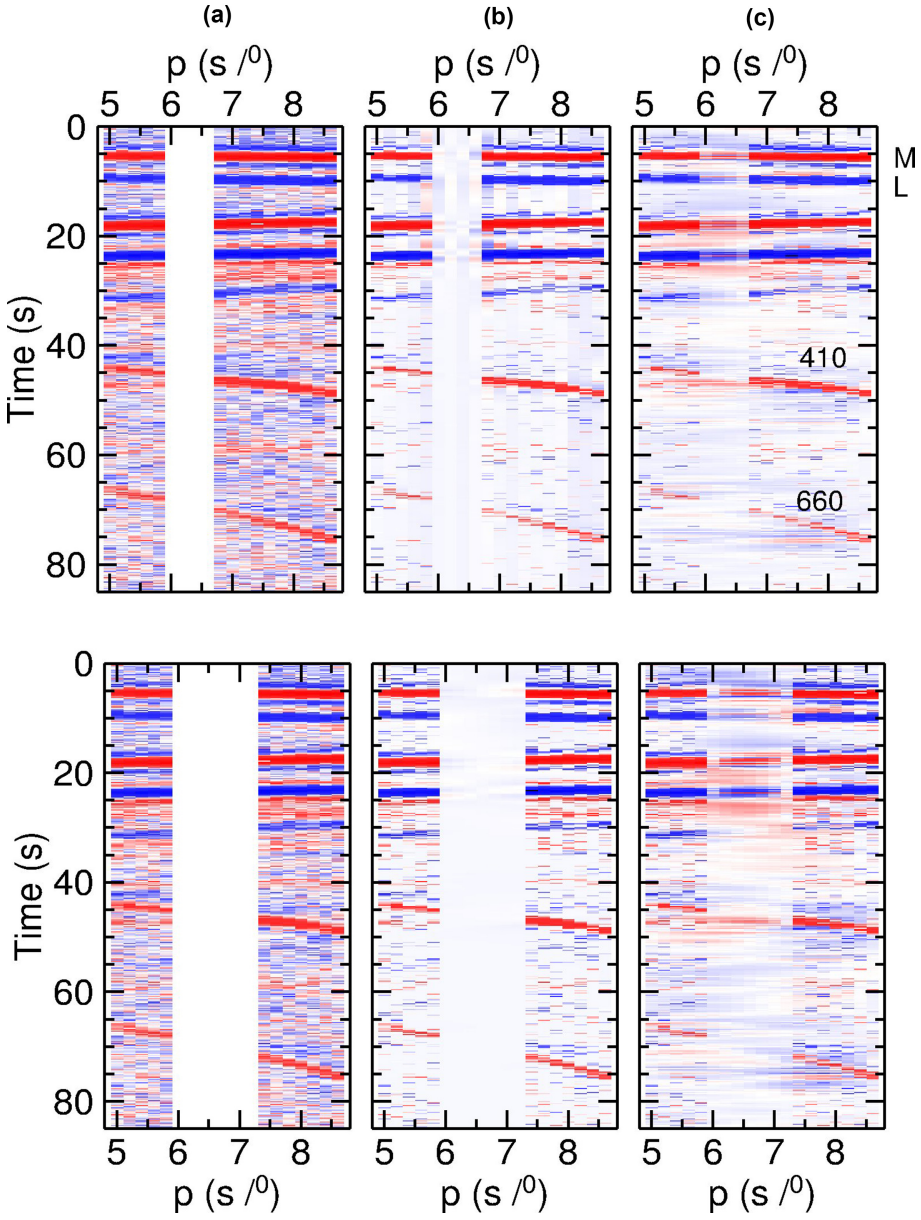

Figure 5. Effect of the spatial sampling density on the ST demonstrated by the same synthetic data shown in Fig. 2a. (a) Images with data gaps of different widths (1.0 s deg^{-1} in the upper panel, 1.6 s deg^{-1} in the lower panel) in the slowness domain. (b) The inverse ST images. (c) Same as (b) but with interpolation. It is clear that the ST can properly reconstruct data with gaps, while the interpolation seems to be ineffective beyond certain data gap and slope (lower panel).

where, r_k is the residual difference between the odd component of data and its prediction from the even component.

Now, the coarse approximation c becomes the new data and the above-mentioned steps are repeated at the next scale level.

Once the data are transformed to the seislet domain, the inverse scheme will be applied to reconstruct the RF amplitude data. The inverse steps consist of reconstruction of the even component following eq. (3),

$$\mathrm{e} = c - U\,[r]\,, \tag{5}$$

and subsequently reconstruction of the odd component following eq. (1),

$$\mathrm{o} = r + P\,[\mathrm{e}]\,. \tag{6}$$

In order to get the information about seislet coefficients the forward ST is required which starts with the finest scale (the original sampling) and go to the coarsest scale as described above. In order to preserve the signal of interest while reconstructing the data, we should apply inverse ST with the coarsest scale and go back to the finest scale (Chen *et al.* 2014). However, for reconstructing a high-resolution image the seislet forward transform accommodates with the most important de-noising approach called thresholding. So, in this study, in order to reduce the noise coefficients for reconstructing the RF amplitudes the significant signal coefficients are preserved. Here we adopted the soft thresholding approach (Donoho 1995) for limiting the significant coefficients and its operator is defined as

$$T_\tau(x) = \begin{cases} (|x| - \tau) * \mathrm{sign}(x) & \text{for } |x| \geq \tau \\ 0 & \text{for } |x| < \tau \end{cases},$$

where 'sign' is the signum function, x stands for seislet coefficients and τ is the threshold value. The thresholding scheme is based on the assumption that noise in the ST is Gaussian and approximately

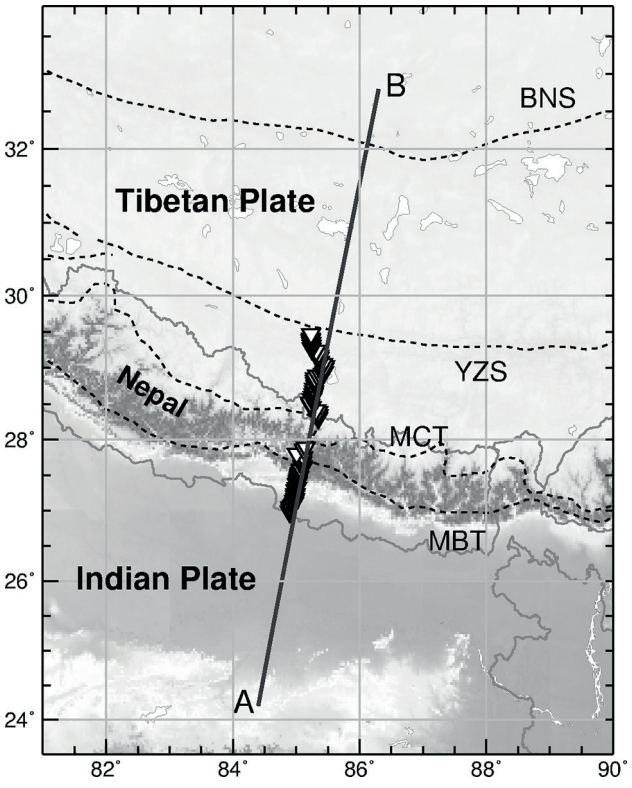

Figure 6. Location map of the seismic stations (inverted white triangles with thin black border). Major thrusts and suture zones are plotted on the map (black dotted lines). MBT, Main Boundary Thrust; MCT, Main Central Thrust; YZS, Yarlung Zangbo suture; BNS, Bangong-Nujiang Suture. AB—location of a seismic profile along which the RF migration and ST are performed.

stationary at each resolution level. This follows from the fact that the seislet basis is orthogonal. Further, the thresholds affect the RF amplitude and the transform compresses the data/image along the local structures. While for noisy data or data with conflicting dips, the threshold value for the ST should be chosen up to a certain limit so that it will not bring any harm to the signal of interest otherwise it may limit the compression ratio of the ST. Such compression can lead to reconstruction errors while taking the inverse transform (Donoho & Johnstone 1994). However, finding an optimized/exact value for soft thresholding is little time consuming in practice but efficient enough to provide the suitable de-noising results. In order to set the optimum threshold, we use a percentile strategy of Chen *et al.* (2014), assuming that a certain percentage of coefficients can represent the RF data. The percentile thresholding refers to using a constant percentage of maximum coefficients during the iterations. In order to obtain a very good reconstruction, the number of iterations should be relatively large (here we took about 120 iterations). During each iteration, we preserve the coefficients as mentioned in each figure. After the iterations are completed, we obtain a well-reconstructed data visually verified with a high SNR, here, for example, we have the SNR derived from noise-free and de-noised signal of about 7 dB for station HYB. For the field data example, as we do not know the exact answer, we cannot judge by numerical measurement. Instead, we only evaluate by visual observation, which is still effective. For example, if we choose a threshold of 20%, we preserve the 80% largest coefficients attributable to signal for reconstruction of the image. Then, when tuning the parameters, we can only tune the percentage, which is convenient to implement in practice.

3 APPLICATION TO SYNTHETIC DATA

First, we analyse a synthetic receiver function data set in the ST domain. We used a simple model with Moho, a low-velocity layer and upper-mantle discontinuities (shown in Fig. 1). The synthetic RFs are computed for the epicentral distance range of 30°–90°. The synthetic seismograms have been generated using the reflectivity technique (e.g. Fuchs & Muller 1971; Kind 1985), where full waves are allowed to generate both primary and multiple phases. The source here used to generate the synthetics is a double couple strike-slip. For the synthetic case, the receiver functions have been computed as follows. First of all, the vertical and horizontal components have been rotated to the L and Q components along and perpendicular to the ray direction, respectively, using the estimated maximum polarization direction of the *P* wave based on the maximum eigenvalue of the covariance matrix. Then the L component has been deconvolved from the respective Q component to get the receiver functions. Here, we have adopted the time-domain deconvolution technique (Berkhout 1977). Prior to deconvolution, the data have been filtered with Butterworth low pass filter of corner frequency of 0.5 Hz. The image of the synthetic RF and the models are displayed in Fig. 1. The image has been generated with stacks in a narrow slowness bin of 0.2 s deg^{-1}. As described in the Methodology section, the ST has been computed with a threshold value of 20% with the amplitude of RF as input. This numerical value for thresholding has been reached after exploring many other values, where most of our phases are optimally resolved. Once the forward ST has been done, for the purpose of reconstruction of the image the inversion has been estimated with the same regularization parameters as used during forward ST. The results of forward ST and inversions have been displayed in Figs 1c and d, respectively. From Fig. 1c, it is clear that the seislet coefficients decay rapidly as the amplitude of coefficient get diffused after the scale around 4. Here, we are using the RF data as input with three columns having time, slowness and amplitude to the forward seislet computation with the method of soft thresholding (Donoho 1995). Once the seislet has been estimated the reconstruction is done by utilizing the most significant seislet coefficients. Fig. 1d shows the reconstructed image, which optimally represents the original input data as the low amplitude, numerical noise and noise introduced by the processing or filtering have been substantially suppressed.

In order to mimic the observed data, we added the Gaussian noise to the RF waveforms. The noisy RF data are analysed in the seislet domain and further reconstructed using inverse-ST. The resulting images for two different scenarios are displayed in Fig. 2. Here 7 and 10% Gaussian noise with mean = 0 are added to the synthetic data and are shown in Figs 2a and b, respectively. The resulting images (Figs 2c and d) show that the desired phases are recovered well in spite of that the phases in the noisy data are visually not very clear.

Fig. 3 depicts synthetic RF for a simple model as shown in Fig. 3a (same as Fig. 1a, but down to a depth of 120 km in the upper most mantle) with Moho and a low velocity layer. The primary converted waves Pms and Pls from Moho and LVL respectively are clearly seen Fig. 3b. Apart from primary conversions, the free surface multiples below 15 s are also generated with greater moveout. To investigate the ability of ST we add 10% Gaussian noise to the synthetic RF and the result is displayed in Fig. 3c. The inverse ST (in Fig. 3d)

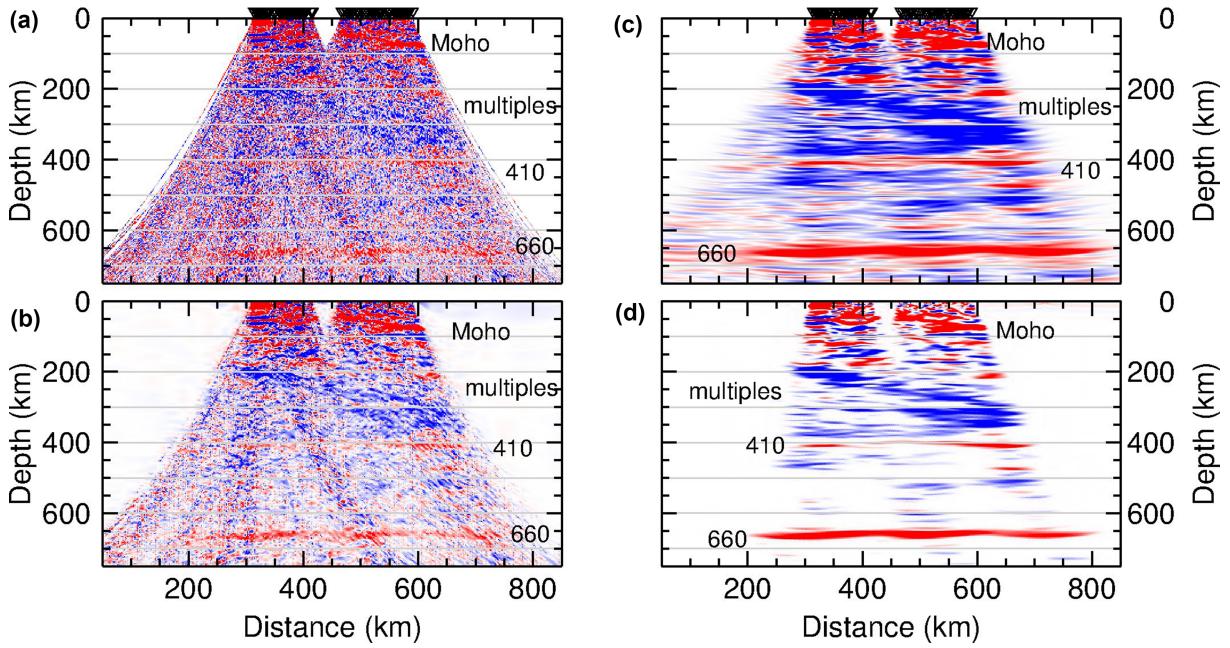

Figure 7. The analysis of observed data along profile AB (shown in Fig. 5) in the seislet domain. (a) The CCP stack of RFs. (c) The Fresnel zone migrated section. The sections cover the upper-mantle depth range. (b and d) Reconstructed images after applying the inverse ST to panels (a) and (c), respectively. It can be seen that the reconstructed images become clearer than the input images.

indicates a significant improvement over the original image. Further, we computed the stack of each subplot in Fig. 3e with bootstrap error (Efron & Tibshirani 1993), for the sake of comparison. In order to estimate error in stacking for each subplot, we employed the bootstrap technique to each set of data by re-sampling 500 times. Each time, we constructed a resampled observed data set (of an equal size to the observed data set) that was obtained by random sampling with replacement from the original data set, and then we stacked resampled seismograms after a moveout correction. Those 500 bootstrap stacked seismograms are then used to estimate the standard error (SE) of the final stacked trace. The reconstructed stack has clear phases similar to the noise free data (e.g. Fig. 3a), whereas the noisy stack (from Fig. 3c) annihilate the prominent phases including the multiples. The stack trace of the reconstructed data, therefore, indicates that the Gaussian noise energy has been attenuated substantially and there is significant improvement of the SNR. Additionally, in this figure it is also obvious that the amplitude of the stack trace of the reconstructed data shown on the right in Fig. 3e differ from the other two traces because during the inverse seislet transform the virtual wave field produced by the Gaussian noise gets diminished as a result of which higher amplitude signal will primarily control the gain function. So, in response to the low intensity portion of the signal the gain will increase in reaction to the diminished overall noise wavefield. This increase in gain consequently boosts the lower level signal and allows these lower level boosted signals to get added constructively which is present in the noisy data sets as a result of which the appearance of the waveform gets enhanced effectively. The important ramification of this plot is the visual identification of the phases by the interpreter, that is, the noisy trace may lead to something deviated interpretation than the true one; however, the constructed stack may be helpful in such a case.

Fig. 4 demonstrates the application of ST to a migrated receiver function data set, generated for a simple model consisting of Moho, a LVL in the upper most mantle till 120 km depth, while the lower part is taken from the IASP91 model (Fig. 4a). The synthetic data have been generated and processed as described in the previous paragraph. Here, we migrated the RF data into depth domain within the Fresnel zones around each ray path (Kind *et al.* 2002). RF amplitudes were migrated into the cross-section as diffracted waves from single scatterers, so smiley artifacts appear where data coverage is sparse. The station spacing is kept 0.5°. The migrated image shows some spurious (Fig. 4b) phases with smiley effect. The RF data in depth domain are subjected to the seislet domain as mentioned in the earlier section and then inverted to retrieve the image. The reconstructed image after inverse ST is displayed in Fig. 4c, which is much clearer and having only prominent phases corresponding to the input model. Furthermore, Fig. 4c is devoid of any smiley effect which in few cases gives the impression of an extended interface especially in the case of less dense data set. Here we used thresholding value of 15% as discussed in the Methodology section. We can see that after applying the threshold, the output image is quite clearer.

Due to various reasons seismic data may have spatial gaps or missing traces in seismological studies. In order to demonstrate the impact of spatial sampling density on the de-noising performance of the seislet transform, here we use the synthetic data from Fig. 2a and introduce gaps of various widths in slowness domain (Fig. 5). Since the ST has inherent property of de-noising and interpolation, here first we only restrict to de-noising by choosing proper thresholds (Fig. 5b) as discussed in the previous section. Results show that introducing the data gaps do not have significant influence on de-noising nature of the ST. Next, we play with the regularization values. In order to recover the missing signal components at the spatial locations, we use an effective sparse transform, that is, the same ST approach which is accommodated with the local slope. However, in order to recover the missing signal components at the spatial locations we used different thresholding values and regularization parameters iterated several times (around 120) until the missing data are optimally restored (Fig. 5c). It is observed that

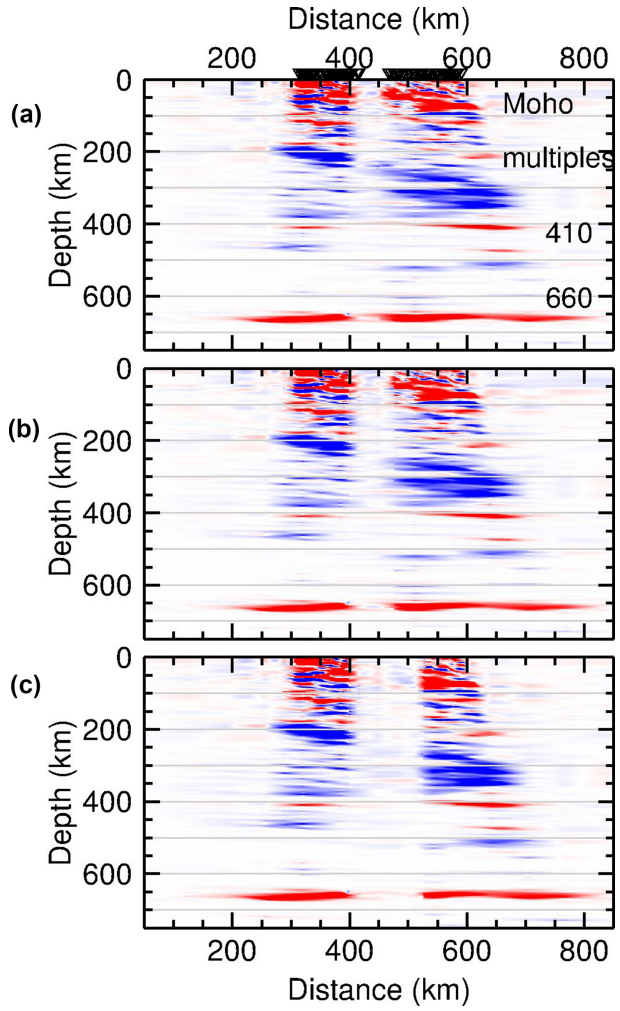

Figure 8. Reconstructed Hi-CLIMB sections by the ST with data gaps of different widths in distance from the original receiver functions. A threshold of 16% has been applied. It is clear that noises are substantially suppressed in spite of gaps in data.

the interpolation is more effective for smaller data gap and the more inclined phases tend to be poorly interpolated.

4 APPLICATION TO OBSERVED DATA

4.1 The Hi-CLIMB network

Synthetic tests have demonstrated that the application of ST substantially improves the SNR of the RF images (converted wave data). Here we test the approach with real data acquired from the HI-CLIMB network in southern Tibet (Nabelek *et al.* 2009; Fig. 6). The seismological experiment was in operation from 2002 to 2005 with an average station spacing of ∼5 km (Nabelek *et al.* 2009). The array covers the foot hill of the Himalayas in Nepal, higher Himalayas and Tibet; however, we restrict our application to the southern part of the profile consisting of 64 broad-band seismic stations (Fig. 6).

Using these data sets, a number of seismological works have been published in the recent past. Nabelek *et al.* (2009) analysed the converted wave technique and studied the lithospheric structures, tracing the Indian Moho till 31°N latitude in Tibet. First, we computed receiver functions (e.g. Kumar & Kawakatsu 2011; Kumar *et al.* 2011) of all the available stations. The final images generated using two different stacking approaches, for example, the common conversion point stacking (CCP) and the Fresnel zone migration are displayed in Figs 7a and c. On application of the ST, the image reconstruction has been taken place by applying 20% thresholding collecting the significant coefficients which helps in compressing the signal and noise along their local slopes. The reconstructed image indicates an excellent improvement over the original in terms of background noises and artifacts (Figs 7b and d, top and bottom panels). However, in the large depth range the re-constructed images are laterally shrunk due to the annihilation of diffused end data of lower amplitude.

We further analysed the impact of the spatial sampling density on the de-noising performance of the seislet transform with the same HI-CLIMB data (Fig. 8). The images are produced by the same Fresnel zone migration stacking procedure as shown in Fig. 7d. Figs 8a–c are the reconstructed results by the inverse ST after data gaps of different widths have been introduced. The experiment shows that, when there is smaller data gap in the input data sets the converted wave signal and noise can be sampled without aliasing which leads to the enhancement of the wavefield continuity (Figs 8a and b). When the data gaps increase the shallow seismic phases are resolved very well and the depth seismic phases with strong dips are still resolved poorly (Fig. 8c) as the seislet transform fills up the deficiency in the input data in its own domain by following the local slopes of the events.

4.2 Geoscope station HYB from the Indian shield

In this section, we examine the performance of the presented method on real data application to HYB, a Geoscope station located in Hyderabad, on the Precambrian craton of the Indian shield. We used the teleseismic earthquake data to compute the receiver functions as described in the previous section (e.g. Kumar & Kawakatsu 2011; Kumar *et al.* 2011). The receiver function image is prepared and presented in Fig. 9a with slowness as abscissa. We observe strong phases at ∼4 s and ∼18–20 s corresponding to the Moho conversion and free surface multiples, which were previously modeled by Saul *et al.* (2000). However, the upper-mantle discontinuities at 410 and 660 km depths are poorly visible. For de-noising this complex data set we have performed the seislet scheme (Figs 9b and c) with 7% and 25% thresholding as the original seismic image would not be optimally sparse so that threshold should be more conservative in order to avoid any possible damage to the signals. The stacks for both the original and reconstructed RFs (Fig. 9d) show all the prominent discontinuities. The stacks are generated after moveout correction for direct conversions with a reference slowness of 6.4 s deg^{-1} (Yuan *et al.* 1997) using IASP91 velocity model (Kennett & Engdahl 1991). It is interesting to note that the P410s and P660s phases, which are not very clearly seen in the individual RF (Fig. 9a), become more visible in the reconstructed images (Figs 9b and c). Apart from these phases, another intriguing phase at about 30 s can be observed (Figs 9b and c) unambiguously. Here for the sake of comparison, we applied two different threshold values. It is clear that the threshold values of 25% (Fig. 9b) and 7% (Fig. 9c) bring out the X-discontinuity; however, a lower value of threshold seems to have slightly less resolution. The SNR in each case is estimated to be about 7 dB. Although all the stacks show more or less similar phases, however, the careful observation shows that the spurious oscillations in RF stacks (the right-hand panel of Fig. 9d) are more due to the random noise compared to the stack of Figs 9b and c

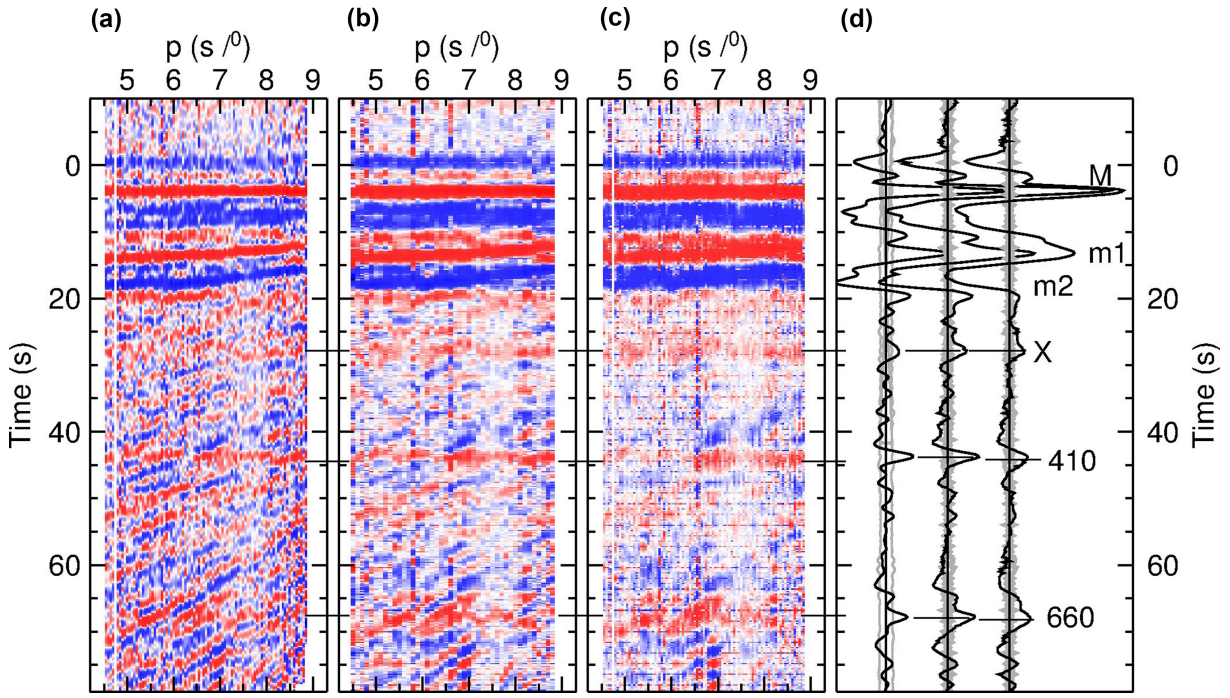

Figure 9. Observed data example from Geoscope station HYB located in the central Indian shield on the Precambrian terrain. The images in panels (a)–(c) are the observed RF and the reconstructed images after inversion of Seislet Transform with two different regularization parameters (thresholding values of 25 and 7, respectively). The purpose of applying different parameters is to show the phase at ∼30 s. The stacks of all the data are shown in (d), that is, the right and left traces correspond to (a)–(c) data, respectively. Two thin lines running on the mean of each stack trace are the standard error of $\pm 2\sigma$. It is clearly seen that the reconstructed image brought out all the prominent phases along with a discontinuity at about 30 s marked as X, which is not prominent in the original receiver function image in (a).

(left trace in Fig. 9d) where the random noises are substantially reduced. Also the linear stacking error is lesser in the reconstructed stack compared to the RF stack. The de-noising result shows an excellent improvement as the mentioned approach has removed most of the random noise due to its better compression capability and improves the SNR.

5 CONCLUSIONS

This study presents the application of a de-noising approach of RF data in the seislet domain to subside the incoherent and Gaussian noise. Tests of synthetic and real field data show a substantial improvement over the original images by suppressing the background random noise and artifacts while preserving the details of the geological structures of interest. The advantage of analysing RF data in the seislet domain is that the converted phases can be identified with more confidence. However, the aliasing of the reconstructed image is influenced by the wide spatial data gap and local slope.

ACKNOWLEDGEMENTS

The director NGRI has kindly permitted to publish this work. Seismic data for Hi-CLIMB and HYB (Hyderabad) are from IRIS (DMC) and Geoscope. Plots are generated using Generic Mapping Tool (Wessel & Smith 1995). The codes used here are from the Madagascar open-source software package freely available at http://www.ahay.org. The manuscript is benefited immensely from the comments by Prof. Chauris (editor), associated editor and two anonymous reviewers. This work has been performed under the Main Lab Project of the Passive Seismology group. B.Dalai is a PhD student working in sponsored by Ministry of Earth Sciences, Govt. of India. The paper has Ref. No. NGRI/LIB/2018/Pub-68.

REFERENCES

Abma, R. & Kabir, N., 2005. Comparison of interpolation algorithms, *Leading Edge,* **24,** 984–989.

Berkhout, A.J., 1977. Least-squares inverse filtering and wavelet deconvolution, *Geophysics,* **42,** 1369–1383.

Burdick, L.J. & Langston, C.A., 1977. Modeling crustal structure through the use of converted phases in teleseismic body-wave forms, *Bull. seism. Soc. Am.,* **67,** 677–691.

Chen, S., Donoho, D. & Saunders, M., 1998. Atomic decomposition by Basis Pursuit, *SIAM J. Sci. Comput.,* **20,** 33–61.

Chen, Y., 2016. Dip-separated structural filtering using seislet thresholding and adaptive empirical mode decomposition based dip filter, *Geophys. J. Int.,* **206**(1), 457–469.

Chen, Y. & Fomel, S., 2018. EMD-seislet transform, *Geophysics,* **83,** A27–A32.

Chen, Y., Fomel, S. & Hu, J., 2014. Iterative deblending of simultaneous source seismic data using seislet-domain shaping regularization, *Geophysics,* **79,** V179–V189.

Claerbout, J.F., 1992. *Earth Soundings Analysis: Processing versus Inversion,* Blackwell Scientific Publications, Inc.

Cohen, A., Daubechies, I. & Feauveau, J.C., 1992. Biorthogonal bases of compactly supported wavelets, *Commun. Pure Appl. Math.,* **45,** 485–560.

Donoho, D.L., 1995. De-Noising via soft thresholding, *IEEE Trans. Inf. Theory,* **41**(3), 631–627.

Donoho, D.L. & Johnstone, I.M., 1994. Ideal spatial adaptation via wavelet shrinkage, *Biomefrika,* **81,** 425455.

Efron, B. & Tibshirani, R., 1993. *An Introduction to the Bootstrap,* Chapman and Hall/CRC.

Fomel, S., 2002. Applications of plane-wave destruction filters, *Geophysics,* **67,** 1946–1960.

Fomel, S. & Liu, Y., 2010. Seislet transform and seislet frame, *Geophysics,* **75**(3), V25–V38.

Foster, D.J. & Mosher, C.C., 1992. Suppression of multiple reflections using the radon transform, *Geophysics,* **57,** 386–395.

Fuchs, K. & Muller, G., 1971. Computation of synthetic seismograms with the reflectivity method and comparison with observations, *Geophys. J. R. astr. Soc.,* **23,** 417–433.

Guo, K. & Labate, D., 2007. Optimally sparse multidimensional representation using shearlets, *SIAM J. Math. Anal.,* **9,** 298–318.

Hermann, F.J., Boniger, U. & Verschuur, D.J., 2007. Non-linear primary-multiple separation with directional curvelet frames, *Geophys. J. Int.,* **170,** 781–799.

Kanasewich, E.R., Hemmings, C.D. & Alpaslan, T., 1973. Nth-root stack nonlinear multichannel filter, *Geophysics,* **38,** 327–338.

Kennett, B.L.N. & Engdahl, E.R., 1991. Traveltimes for global earthquake location and phase identification, *Geophys. J. Int.,* **105,** 429–465.

Kind, R., 1985. The reflectivity method for different source and receiver structures and comparison with GRF data, *J. Geophys.,* **58,** 146–152.

Kind, R. *et al.*, 2002. Seismic images of crust and upper mantle beneath Tibet: evidence for Eurasian plate subduction, *Science,* **298**(5596), 1219–1221.

Kumar, P. & Kawakatsu, H., 2011. Imaging the seismic lithosphere–asthenosphere boundary of the oceanic plate, *Geochem. Geophys. Geosyst.,* **12**(1) .

Kumar, P., Kawakatsu, H., Shinohara, M., Kanazawa, T., Araki, E. & Kiyoshi, S., 2011. *P* and *S* receiver function analysis of seafloor borehole broadband seismic data, *J. geophys. Res.,* **116,** B12308, doi:10.1029/2011JB008506.

Langston, C.A., 1977. Corvallis, Oregon, crustal and upper mantle structure from teleseismic *P* and *S* waves, *Bull. seism. Soc. Am.,* **67,** 713–724.

Liu, W., Cao, S. & Chen, Y., 2016. Seismic time-frequency analysis via empirical wavelet transform, *IEEE Geosci. Remote Sens. Lett.,* **13,** 28–32.

Mallat, S., 2009. Geometrical grouplets, *Appl. Comput. Harmon. Anal.,* **26,** 161–180.

Nabelek, J. *et al.*, 2009. Underplating in the Himalaya–Tibet collision zone revealed by the Hi-CLIMB experiment, *Science,* **325,** 1371–1374.

Neal, S.L. & Pavlis, G.L., 1999. Imaging *P* to *S* conversions with multichannel receiver functions, *Geophys. Res. Lett.,* **26,** 2581–2584.

Pavlis, G.L., 2011. Three-dimensional wavefield imaging of data from the USArray: new constraints on the geometry of the Farallon slab, *Geosphere,* **7,** 785–801.

Poppeliers, C. & Pavlis, G.L., 2003. Three-dimensional, prestack, plane wave migration of teleseismic *P*-to-*S* converted phases, 2. Stacking multiple events, *J. geophys. Res.,* **108,** 2112, doi:10.1029/2001JB001583.

Saul, J., Kumar, M.R. & Sarkar, D., 2000. Lithospheric and upper mantle structure of the Indian shield, from teleseismic receiver functions, *Geophys. Res. Lett.,* **27,** 2357–2360.

Sen, M.K., Biswas, R., Mandal, P. & Kumar, P., 2014. Basis pursuit receiver function, *Bull. seism. Soc. Am.,* **104,** 2673–2682.

Sheldrake, K.P., Marcinkovich, C. & Tanimoto, T., 2002. Regional wavefield reconstruction for teleseismic *P*-waves and surface waves, *Geophys. Res. Lett.,* **29**(11), 1544.

Starck, J.L., Candes, E.J. & Donoho, D.L., 2002. The curvelet transform for image denoising, *IEEE Trans. Image Process.,* **11–6,** 670–684.

Sweldens, W. & Schroder, P., 1996. Building your own wavelets at home,in *Wavelets in Computer Graphics,* pp. 15–87, eds Klees, R. & Haagmans, R., Springer.

Tessmer, G. & Behle, A., 1988. Common reflection point data-stacking technique for converted waves, *Geophys. Prospect.,* **36,** 671–688.

Vinnik, L.P., 1977. Detection of waves converted from *P* to *SV* in the mantle, *Phys. Earth planet. Inter.,* **15,** 39–45.

Wessel, P. & Smith, W.H.F., 1995. New version of the generic mapping tools released, *EOS, Trans. Am. geophys. Un.,* **76,** 329.

Xue, Y., Ma, J. & Chen, X., 2014. High-order sparse radon transform for AVO-preserving data reconstruction, *Geophysics,* **79,** V13–V22.

Xue, Y., Yang, J., Ma, J. & Chen, Y., 2016. Amplitude-preserving nonlinear adaptive multiple attenuation using the high-order sparse radon transform, *J. geophys. Eng.,* **13**(3), 207–219.

Xue, Z., Zhu, H. & Fomel, S., 2017. Full waveform inversion using seislet regularization, *Geophysics,* **82**(5), A43–A49.

Yilmaz, O., 2001. *Seismic Data Analysis,* Society of Exploration Geophysicists.

Yuan, X., Ni, J., Kind, R., Mechie, J. & Sandvol, E., 1997. Lithospheric and upper mantle structure of southern Tibet from a seismological passive source experiment, *J. geophys. Res.,* **102,** 27 491–27 500.

Zhang, J.H. & Zheng, T., 2015. Receiver function imaging with reconstructed wavefields from sparsely scattered stations, *Seismol. Res. Lett.,* **86,** 165–172.